CHINESE OPTICS LETTERS

Vol. 19, No. 12 | December 2021

High period frequency LIPSS emerging on 304 stainless steel under the irradiation of femtosecond laser double-pulse trains

Yifei Li (李抑非)[1], Jie Hu (胡 洁)[1*], Wei Liu (刘 威)[1], Jiangang Yin (尹建刚)[2], and Jiangang Lu (卢建刚)[2]

[1] Laser Micro/Nano Fabrication Laboratory, School of Mechanical Engineering, Beijing Institute of Technology, Beijing 100081, China

[2] Han's Laser Technology Industry Group Co., Ltd., Shenzhen 518126, China

*Corresponding author: jiehu2@bit.edu.cn

Received April 6, 2021 | Accepted May 17, 2021 | Posted Online September 14, 2021

In this work, we used femtosecond laser double-pulse trains to produce laser-induced periodic surface structures (LIPSS) on 304 stainless steel. Surprisingly, a novel type of periodic structure was discovered, which, to the best of our knowledge, is the first in literature. We surmised that the cause for this novel LIPSS was related to the weak energy coupling of subpulses when the intrapulse delay was longer than the thermal relaxation time of stainless steel. Furthermore, we found that the fluence combination and arrival sequence of subpulses in a double-pulse train also influenced LIPSS morphology.

Keywords: femtosecond laser; laser-induced periodic surface structures morphology; stainless steel.
DOI: 10.3788/COL202119.123801

1. Introduction

Laser-induced periodic surface structures (LIPSS)[1], also termed ripples, are a universal phenomenon. They occur when a linearly polarized laser of appropriate fluence is irradiated on virtually any material, including dielectrics[2–4], semiconductors[5,6], metals[7–9], and recently researched 2D materials[10]. LIPSS were initially discovered by Birnbaum *et al.*[11] in 1965 and have attracted increasing attention, especially after the 1990s thanks to the increasing availability of ultra-short pulsed lasers. LIPSS have application in numerous fields, such as structural coloration[12,13], wettability[14], tribology[8], surface enhanced Raman scattering substrates[15], and biomedicine[16].

The function of an LIPSS-covered surface is dependent on the morphology of the LIPSS. In general, LIPSS are of two types depending on their morphology: low-spatial-frequency LIPSS (LSFL)[11] and high-spatial-frequency LIPSS (HSFL)[11]. LSFL and HSFL are distinguished by spatial period: for LSFL, the period (Λ) lies within a range between the incident laser wavelength λ and half that wavelength ($\lambda/2 < \Lambda < \lambda$); for HSFL, the period is shorter than half the wavelength ($\Lambda < \lambda/2$). The morphology of LIPSS formed after laser irradiation intrinsically depends on the interaction between the incident laser and material. Currently, it is generally accepted that during the formation of LSFL, key roles are played by excited surface plasmon polaritons (SPPs) and by the interference of the incident laser beam with a surface electromagnetic wave on a rough surface[17–19]. However, the mechanism through which the HSFL forms remains disputed, and several competing theories have been proposed, including those of second harmonic generation[20], self-organization[21], and Coulomb explosion[22].

In actual processing, LIPSS morphology can be directly regulated by laser parameter adjustment, such as laser wavelength[23,24], pulse duration[25], fluence[7,26], polarization[5,27], pulse number[6,28], adoption of a single-pulse or double-pulse train[29,30], and interpulse time delay (for a double-pulse train)[31,32]. As a widely applied category of metal materials, stainless steel is frequently used in research on LIPSS morphology control. For example, Yao *et al.*[33] obtained multiple LIPSS morphologies induced by a femtosecond laser on 301L stainless steel under different laser fluences and scanning speeds, and an array of efficient diffractive nanogratings was produced using LIPSS with optimal morphology. Fraggelakis *et al.*[34,35] analyzed the use of stainless steel with respect to variations in laser fluence, pulse delay, and the polarization states of subpulses, and those authors reported on the formation of a new type of triangular structure termed 2D-LIPSS. Thus far, most related studies have focused on controlling LIPSS morphology using either (but not both) single- or double-pulse train irradiation.

In this work, we achieved control of LIPSS morphology on 304 stainless steel under double-pulse train irradiation. We applied subpulses of different fluences in an experiment to explore the effect of an unevenly distributed double-pulse train on LIPSS. Notably, when double-pulse irradiation was applied, a novel periodic structure comprising nanostripes and nanodroplets emerged; we are, to the best of our knowledge, the first to report on this intriguing phenomenon. We posit a qualitative

explanation that this phenomenon is due to the weak energy coupling of subpulses at large intrapulse delays.

2. Experimental Setup

The experimental setup is illustrated in Fig. 1. In our experiments, a commercial chirped-pulse Ti:sapphire regenerative oscillator-amplifier laser system (Spitfire, Spectra-Physics Inc., USA), was used to generate a Gaussian-shaped femtosecond laser beam with a central wavelength of 800 nm, pulse duration of 35 fs, and maximum repetition rate of 1 kHz. Typically, a single-pulse train is adopted, but, when a double-pulse train is required, a beam splitter (in the form of a Michelson interferometer) is added to split the original laser beam emitted by the laser system into two beam arms, with the length of one arm being fixed and the length of the other arm being adjustable through a single-axis translation stage. Through such a setup, the interpulse time delay can be adjusted. To allow the fluences of the two arms to be tuned independently, an attenuator was placed in the path of each of the two arms. A half-wave plate was placed in the optical path to control the polarization orientation of the synthesized laser beam. The single-facet-polished 304 stainless steel samples (15 mm × 15 mm × 1 mm) were mounted on a six-axis translation stage (M-840.5DG, PI, Germany), which has a positional accuracy of 1 μm in both the x and y directions. A 5 times spherical objective lens (NA = 0.15) is used to focus the laser beam onto the sample surface, and the laser beam diameter before entering the objective lens is set as 5 mm. Prior to the experiments, the diameter of the focused Gaussian beam spot (defined by a $1/e^2$ point at the waist) was measured and

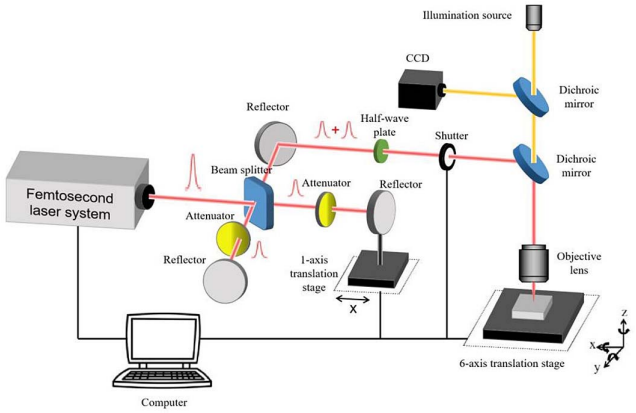

Fig. 1. Experimental setup with two beam arms.

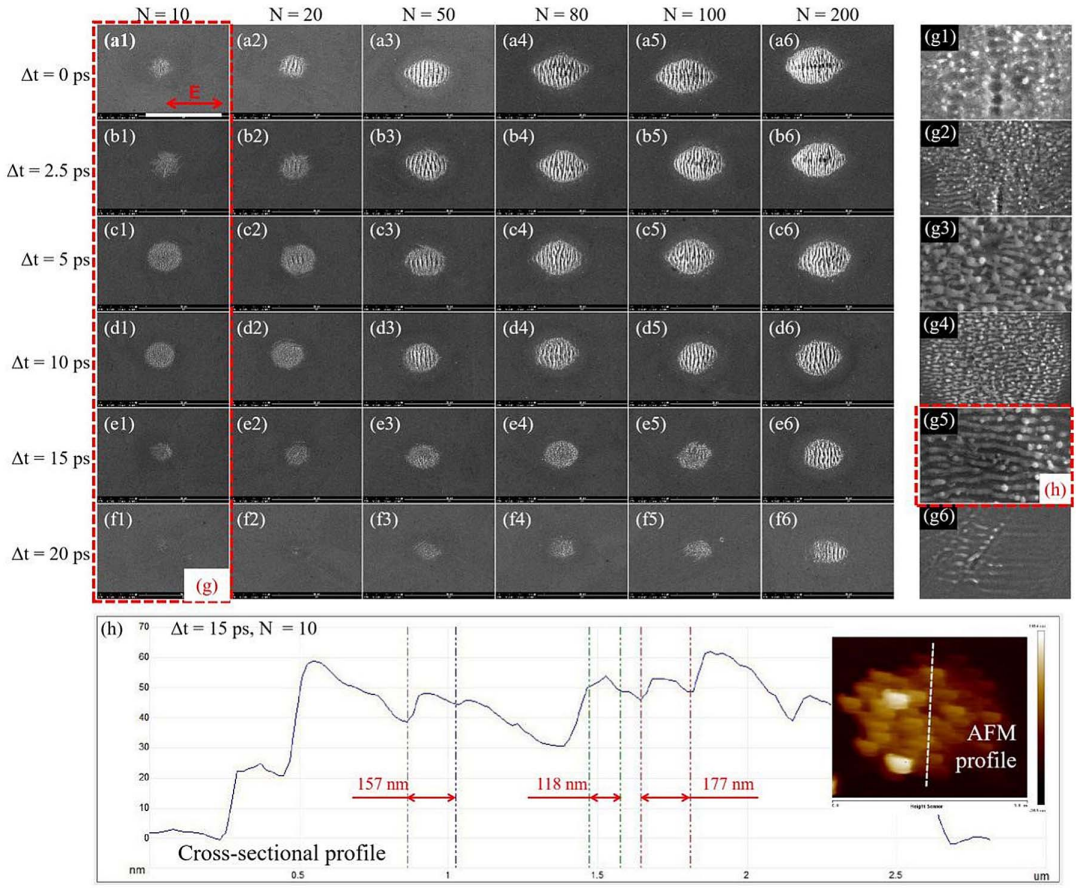

Fig. 2. Total fluence of double-pulse train: 0.388 J/cm^2. Fluence of each subpulse: 0.194 J/cm^2. (a)–(f) SEM images of LIPSS spots at different pulse delays Δt and pulse numbers N. (g) Magnifications of (a1)–(f1). (h) AFM-characterized cross-sectional profile of the structure in panel (g5); the orientation of the cross section is marked in the top-right corner. Laser polarization is indicated in (a1). Scale bar: (a)–(f), 10 μm; (g) is not to scale.

calculated to be ≈8 μm, per the method proposed by Liu[36]. All experiments were conducted in air under atmosphere pressure and at room temperature. After processing, the samples were rinsed in an ethanol ultrasonic bath for 10 min to remove the debris from the sample surfaces. The characterization methods used included optical microscopy, scanning electron microscopy (SEM; FEG 250, Quanta, USA), and atomic force microscopy (AFM; Dimension Edge, Bruker, USA).

Firstly, a series of LIPSS spots was obtained under different fluences and pulse numbers using a double-pulse train, and, in this study, the fluence was calculated using the following formula of peak laser fluence:

$$F_p = \frac{2E_p}{\pi\omega_0^2}, \tag{1}$$

where E_p is the energy of a single-laser pulse, and ω_0 is the radius of the laser spot at the waist (≈4 μm for our case). It is noteworthy here that as we adopted a Gaussian-shaped femtosecond laser beam, the intensity of the laser pulse varied with time and the peak fluence calculated by Eq. (1) was a time-averaged value. We used this time-averaged fluence in order to facilitate the reproduction of the experimental results demonstrated in this work; if any researcher concentrated on the exact relationship between the peak fluence and the morphology of LIPSS, he/she needs to pay more effort to retrieve the exact temporal and spatial profile of the laser pulse. In addition, stainless steel has an initial reflectance of approximately 60% at an 800 nm central wavelength, which means that the energy coupled into the material by absorption should be significantly less than the nominal amount and that the calculated fluence values are not equal to the energy values applied via laser irradiation.

As mentioned, most studies have focused on manipulating LIPSS morphology using irradiation by either (but not both) single-pulse or double-pulse trains; in this work, we used double-pulse trains.

3. Experiments and Discussions

Figure 2 illustrates the evolution of an LIPSS spot with given pulse numbers under the irradiation of a 0.388 J/cm^2 double-pulse train. As depicted in Figs. 2(a)–2(f), with an increased pulse delay Δt, LIPSS formation became increasingly difficult, and almost no structure was generated, as shown in Fig. 2(f1). This was because of a long pulse delay, where the electrons excited by the first subpulse had faded when the second subpulse arrived. This in turn meant that the overall effect of the pulse train was weaker than that of a pulse train with a short pulse delay, which hindered LIPSS formation. Moreover, we discovered a notable phenomenon: when Δt was between 5

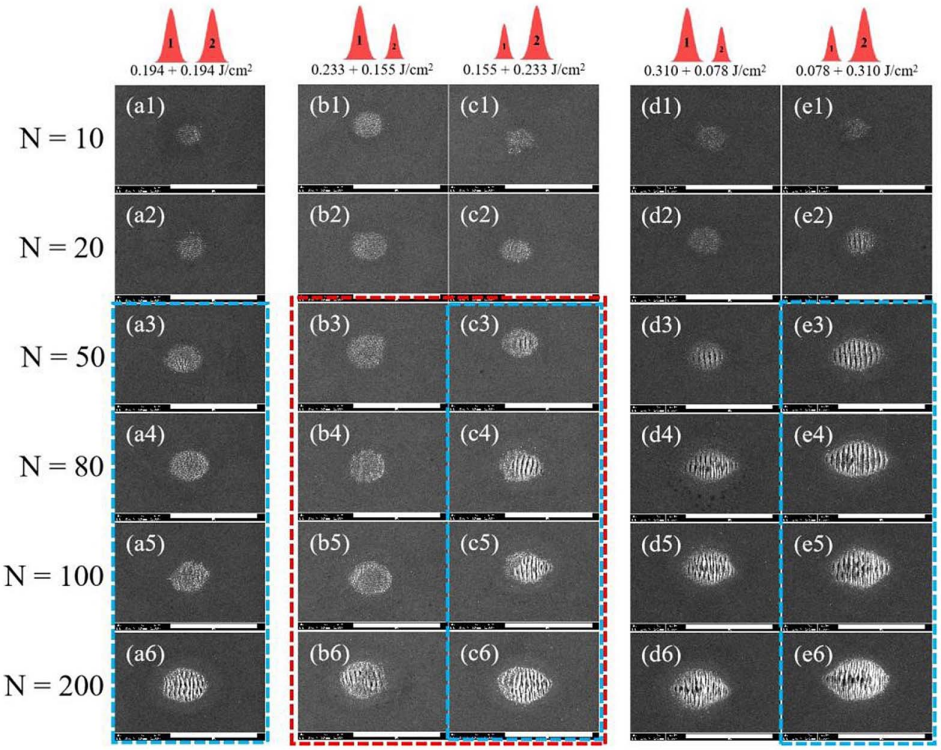

Fig. 3. Total laser fluence of double-pulse train was fixed at 0.388 J/cm^2, and pulse delay Δt was maintained at 15 ps. Variation of LIPSS morphology in relation to pulse number under the following subpulse fluence combinations: (a) 0.194 + 0.194 J/cm^2 (with 1:1 intrapulse energy ratio), (b) 0.233 + 0.155 J/cm^2 (3:2), (c) 0.155 + 0.233 J/cm^2 (2:3), (d) 0.310 + 0.078 J/cm^2 (4:1), and (e) 0.078 + 0.310 J/cm^2 (1:4). The only difference between (b) and (c) as well as (d) and (e) lies in their reversed subpulse arrival sequences. Morphology variation with the fluence combination is marked by the blue dotted rectangles. Morphology variation with subpulse arrival sequence is marked by the red dotted rectangle. Scale bars: 10 μm.

and 15 ps, a special type of high-spatial-frequency periodic structure was formed on the sample surface prior to the emergence of the LIPSS. Figures 2(a1)–2(f1) depict the evolution of this special structure, and the magnified images are shown in Figs. 2(g1)–2(g6). As depicted in Figs. 2(g1)–2(g6), as the pulse delay increased, the disordered corrugations and pits were gradually replaced by well-organized nanostripes that were parallel to the direction of laser polarization, which had sporadic nanodroplets scattered around them. When $\Delta t = 15$ ps [Fig. 2(g5)], the nanostripes became very clear and well aligned. AFM characterization was conducted on this special structure [Fig. 2(h)], and the findings indicated that the nanostripes had a width of mainly 100 to 200 nm and height approximately in the tens of nanometers. These dimensions clearly distinguished the nanostripes from the HSFL. This special structure could only be obtained by using a double-pulse train and at the proper Δt value. We are, to the best of our knowledge, the first to report this finding.

We observed that the nanostripes began to appear when Δt was 5 ps, which was close to the thermal relaxation time τ_{eq} of stainless steel (5.1 ps)[37]. Thus, we supposed that the formation of this special structure was related to the energy transfer between the electron and the lattice system. Specifically, when a double-pulse train with a pulse delay greater than τ_{eq} is irradiated on the sample surface, the first subpulse arrives at the surface first and energizes the electrons; subsequently, the electron–lattice system reaches a thermal equilibrium after a time interval τ_{eq}. Thereafter, the second subpulse steps in, and extra energy is injected into the electron system and directly flows into the lattice system, interrupting the as-established equilibrium; under this condition, the overall coupling effect of the subpulses is weaker than those with pulse delays shorter than τ_{eq}, and the hydrodynamical behavior of the material is altered. Finally, LIPSS cannot be formed due to the weak coupling of subpulses, and the special structure is generated by the altered hydrodynamical behavior.

Mitko *et al.*[38] reported the appearance of a type of HSFL when irradiating sample with a 515-nm wavelength, 7-ps pulse duration Yb:YAG laser, and this type of HSFL had a spatial periodicity of around 120 nm, which was close to the special structure reported by our group. Nevertheless, the HSFL reported by Mitko *et al.* was generated under the irradiation of a single-pulse train, and the morphology of them was arbitrarily scattered on the sample surface, while our structure was well-organized, and there were clear nanodroplet-like structures lying around the nanostripes. Henceforth, the two types of HSFL were different from each other.

Subsequently, we attempted to control the LIPSS morphology by adopting different combinations of subpulse fluences and arrival sequences. As shown in Figs. 3(a3)–(a6), 3(c3)–3(c6), and 3(e3)–3(e6), the LIPSS morphology varied with the fluence combination. In Figs. 3(a3)–3(a5), only the aforementioned

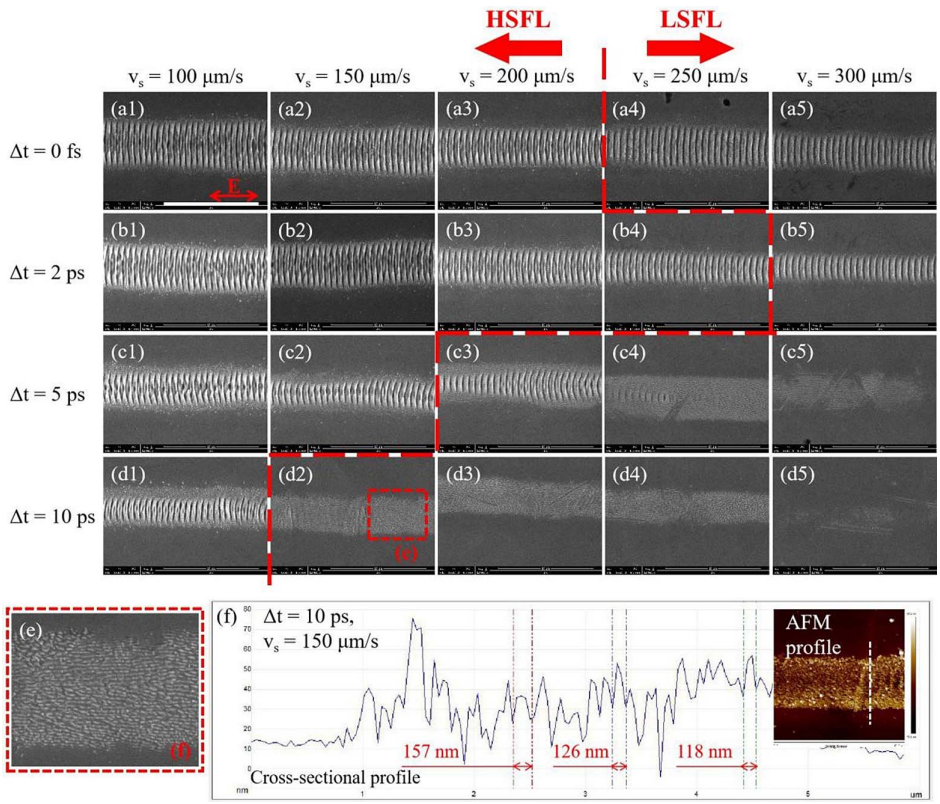

Fig. 4. Total fluence of double-pulse train: 0.544 J/cm^2. Fluence of each subpulse: 0.272 J/cm^2. (a)–(d) SEM images of LIPSS lines at different pulse delays Δt and scanning speeds v_s. (e) Partially enlarged view of (d2). (f) Cross-sectional profile of the structure in panel (e) characterized by AFM, and the orientation of the cross section is marked in the top-right corner. Laser polarization is indicated in (a1). Scale bar: (a)–(d), 10 μm; (e), not to scale.

special periodic structure appeared, whereas LIPSS were formed in Figs. 3(c3)–3(c5) and in Figs. 3(e3)–3(e5). Although the LIPSS were formed in Fig. 3(a6), the size of the spot was relatively small. A previous study[39] revealed that when a double-pulse train is used to generate LIPSS on a silicon surface, the orientation and morphology are determined by the subpulse with the greater fluence. Similarly, in our study, the second subpulse in Fig. 3(e) had a much higher fluence (0.310 J/cm^2) relative to its counterparts in the two other combinations (0.194 J/cm^2 and 0.233 J/cm^2) and thus had a better likelihood of inducing LIPSS generation. Therefore, the greater the disparity between two subpulse fluences is, the more the double-pulse train promotes LIPSS formation. In Figs. 3(b), 3(c) and 3(d), 3(e), two fluence combinations (0.155 + 0.233 J/cm^2 and 0.078 + 0.310 J/cm^2) were selected with their subpulse arrival sequences reversed for us to explore the corresponding effect on LIPSS morphology. The results indicated that at 0.155 + 0.233 J/cm^2, LIPSS formation is better aided by the subpulse with the lower fluence arriving before [Fig. 3(c)] rather than after [Fig. 3(b)] its counterpart with the higher fluence. However, this result did not hold indefinitely, as indicated by the small difference between the LIPSS spots in Figs. 3(d) and 3(e). We posit that this was due to the dependence of electron dynamics on arrival sequence: if the stronger subpulse arrives first, high-density electrons are excited, which, to some extent, shields the subsequent weaker subpulse and, in turn, weakens the coupling between subpulses. Subsequently, when the coupling between subpulses is weak, the pulse train is rendered useless, which results in the formation of a special periodic structure rather than LIPSS.

Subsequently, we analyzed the morphology of the LIPSS line that was generated by a double-pulse train. Because the line could only be formed within a narrow scanning speed range

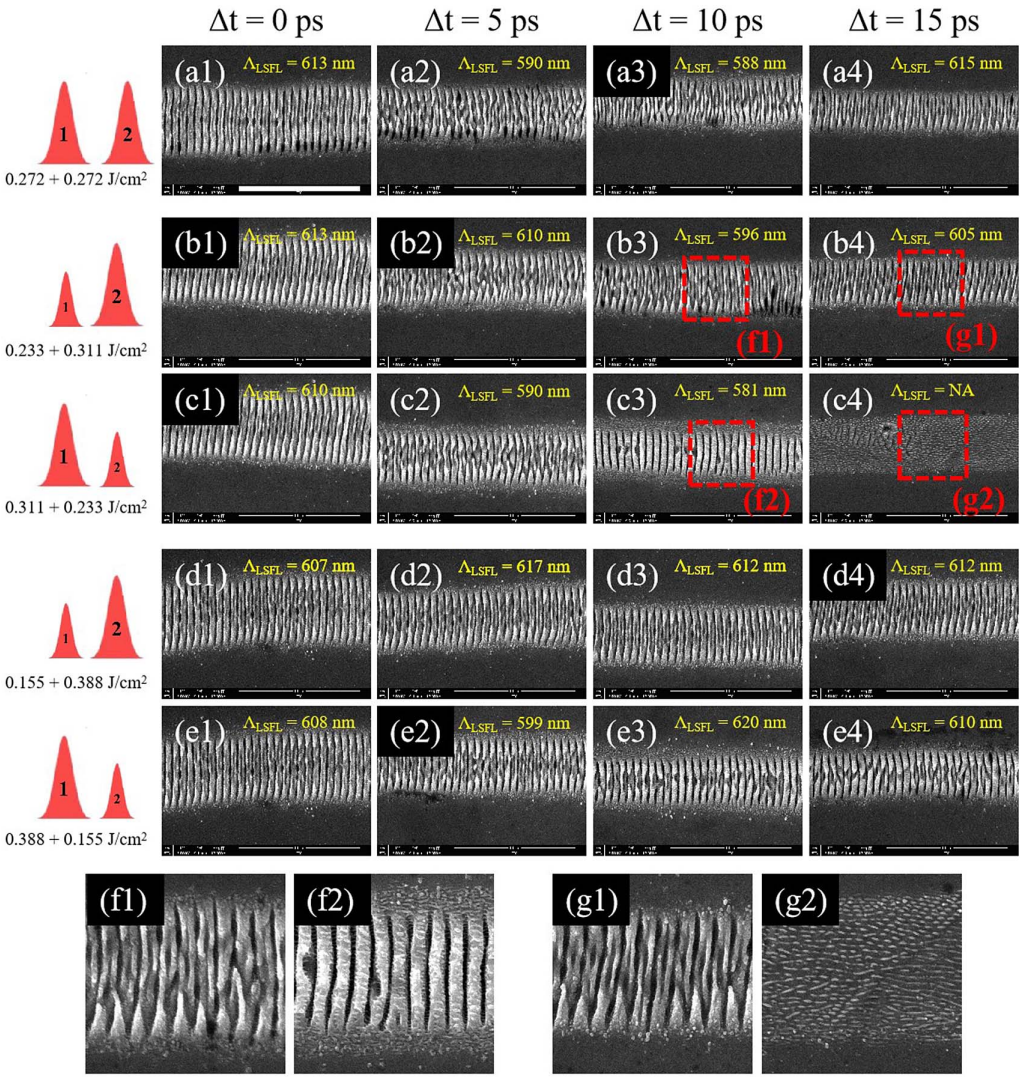

Fig. 5. Total laser fluence of the double-pulse train was fixed at 0.544 J/cm^2, and the scanning speed v_s was maintained at 100 μm/s. SEM images of LIPSS line under the following subpulse fluence combinations: (a) 0.272 + 0.272 J/cm^2 (with 1:1 intrapulse energy ratio), (b) and (c) 0.233 + 0.311 J/cm^2 (3:4) with reversed pulse arrival sequences relative to each other, and (d) and (e) 0.155 + 0.388 J/cm^2 (2:5) with reversed pulse arrival sequences relative to each other. (f1), (f2) and (g1), (g2) are partial magnifications of the areas in (b3),(c3) and (b4),(c4). Scale bar: (a)–(e), 10 μm, marked in (a1); (f) and (g), not to scale.

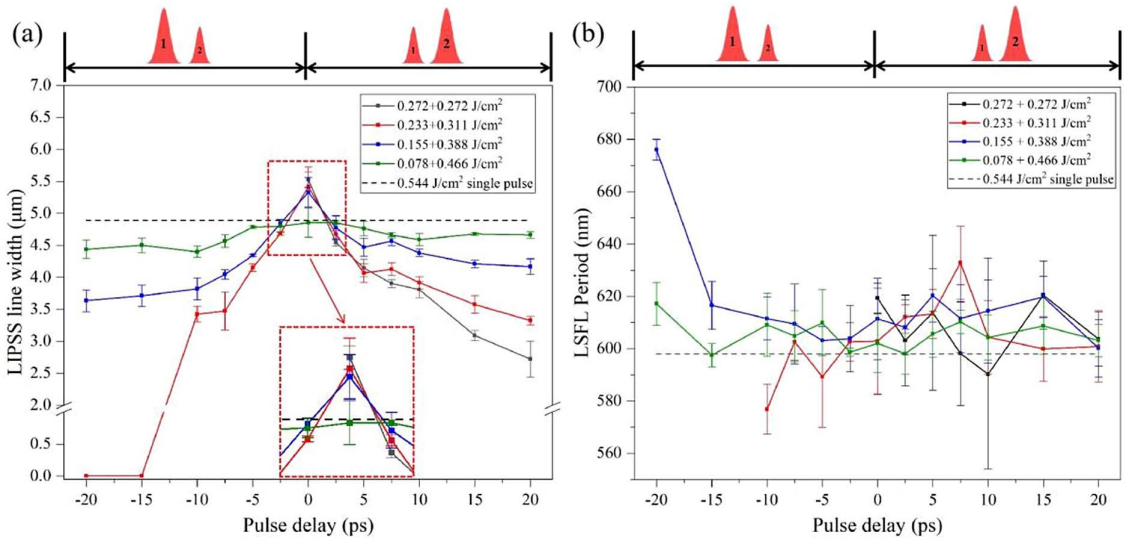

Fig. 6. Total laser fluence was 0.544 J/cm^2, and scanning speed v_s was maintained at 100 μm/s. (a) LIPSS line width as a function of pulse delay under different intrapulse energy ratios, magnification at approximately Δt = 0 ps is presented. (b) LSFL period as a function of pulse delay under different subpulse fluence combinations. A negative pulse delay means that the subpulse arrival sequence is reversed. The LSFL period under the 0.544 J/cm^2 single-pulse mode is also indicated in both (a) and (b) by a dotted line.

at $F_p = 0.388\ \mathrm{J/cm^2}$, we fixed the total fluence of the double-pulse train to be 0.544 J/cm^2 and distributed the fluence evenly to each of the subpulses; the SEM images of the lines are presented in Fig. 4. As presented in Figs. 4(a)–4(d), the speed of transition from HSFL to LSFL decreased with an increase in pulse delay Δt. We deduce that increasing Δt plays a similar role as decreasing total fluence does, which corroborates our supposition that increasing Δt weakens the coupling between the two subpulses. In addition, the special periodic structure observed in Fig. 2 also appeared here [Fig. 4(d2)], and we characterized its profile using AFM. As shown in Fig. 4(f), the geometry of the nanostripes was basically identical to that in Fig. 2(h).

Different combinations of subpulse fluences (together with reversed subpulse arrival sequences) were also applied to the control of LIPSS morphology through the alteration of scanning parameters. Altering the fluence combination resulted in the following characteristics (Fig. 5). The morphology of the LIPSS line remained unchanged when the fluences of subpulses were equal [Fig. 5(a)] or very different [Figs. 5(d) and 5(e)] but changed when the fluences differed slightly [Figs. 5(b) and 5(c)]. Two notable phenomena were also observed. First, as illustrated in Figs. 5(b3) and 5(c3), HSFL and LSFL were formed when the subpulse with lower fluence arrived before and after the subpulse with the higher fluence, respectively. Second, when the pulse delay increased from 10 ps [Fig. 5(c3)] to 15 ps [Fig. 5(c4)], the special structure was formed instead of the LSFL, whereas the structure in Fig. 5(b4) remained similar to the one in Fig. 5(b3). The corresponding magnifications are shown in Figs. 5(f) and 5(g). These two phenomena can be explained by our two explanations posited in the preceding sections of this paper. Specifically, for the structures illustrated from Fig. 5(b3) to Fig. 5(c3), when the subpulse arrival sequence was reversed, the electron dynamics was altered, which eliminated the transition from LSFL to HSFL, leaving only LSFL. Furthermore, for the structures illustrated from Fig. 5(c3) to Fig. 5(c4), as Δt was increased, the coupling between the two subpulses became weak to the point where the LSFL disappeared, and only the special structure was left.

To quantitatively illustrate the morphological variation in Fig. 5, the LIPSS line width and the LSFL period as a function of the pulse delay are presented in Fig. 6. As shown in Fig. 6(a), the line width culminated at $\Delta t = 0$ ps for all fluence combinations (even larger than the line width under single-pulse train irradiation) and then consistently decreased with an increase in pulse delay. However, the trend at which the line width decreased tended to pacify when the fluence disparity between the two subpulses was greater, which was likely to have occurred because the strong subpulse dominated the line formation process. The LIPSS disappeared when $\Delta t \leq -15$ ps for the fluence combination of $0.233 + 0.311\ \mathrm{J/cm^2}$, corresponding to Fig. 5(c4). In Fig. 6(b), the LSFL period continually fluctuated and did not exhibit a clear tendency, but the LSFL obtained under double-pulse train irradiation generally had larger periods than those formed under single-pulse train irradiation. The only extraordinary phenomenon presented in Fig. 6(b) was that the period sharply increased at $\Delta t = -20$ ps for the subpulse fluence combinations of $0.155 + 0.388\ \mathrm{J/cm^2}$ and $0.078 + 0.466\ \mathrm{J/cm^2}$; this sudden increase may be related to the weak coupling of subpulse energy at long pulse delays; more studies are required to verify this relationship.

4. Conclusion

In this study, femtosecond laser double-pulse trains were applied to generate LIPSS on the surface of 304 stainless steel,

and a novel type of periodic structure was observed when the intrapulse delay was between 5 and 15 ps. The mechanism accounting for the formation of this kind of LIPSS was owed to the weak energy coupling of subpulses at large intrapulse delays. Moreover, various combinations of subpulse fluence were adopted so as to observe their influence on the morphology of LIPSS formation. The experimental results of this study indicated that under double-pulse trains, LIPSS formation could be controlled by intrapulse delay, subpulse fluence combination, together with subpulse arrival sequences.

Acknowledgement

This work was supported by the National Key R&D Program of China (No. 2018YFB1107200) and the National Natural Science Foundation of China (Nos. 51675048 and 11704028).

References

1. M. Birnbaum, "Semiconductor surface damage produced by ruby lasers," J. Appl. Phys. **36**, 3688 (1965).
2. Z. Fang and J. Shao, "Femtosecond laser-induced periodic surface structure on fused silica surface," Optik **127**, 1171 (2016).
3. S. Höhm, A. Rosenfeld, J. Krüger, and J. Bonse, "Femtosecond laser-induced periodic surface structures on silica," J. Appl. Phys. **112**, 014901 (2012).
4. T. Jiang, S. Gao, Z. Tian, H. Zhang, and L. Niu, "Fabrication of diamond ultra-fine structures by femtosecond laser," Chin. Opt. Lett. **18**, 101402 (2020).
5. W. Han, L. Jiang, X. Li, P. Liu, L. Xu, and Y. Lu, "Continuous modulations of femtosecond laser-induced periodic surface structures and scanned line-widths on silicon by polarization changes," Opt. Express **21**, 15505 (2013).
6. J. Bonse and J. Krüger, "Pulse number dependence of laser-induced periodic surface structures for femtosecond laser irradiation of silicon," J. Appl. Phys. **108**, 034903 (2010).
7. M. Martínez-Calderon, A. Rodríguez, A. Dias-Ponte, M. Morant-Miñana, M. Gómez-Aranzadi, and S. Olaizola, "Femtosecond laser fabrication of highly hydrophobic stainless steel surface with hierarchical structures fabricated by combining ordered microstructures and LIPSS," Appl. Surf. Sci. **374**, 81 (2016).
8. J. Bonse, R. Koter, M. Hartelt, D. Spaltmann, S. Pentzien, S. Höhm, A. Rosenfeld, and J. Krüger, "Femtosecond laser-induced periodic surface structures on steel and titanium alloy for tribological applications," Appl. Phys. A **117**, 103 (2014).
9. B. Wu, C. Wang, Z. Luo, J. Li, S. Man, K. Ding, and J. A. Duan, "Controllable annulus micro-/nanostructures on copper fabricated by femtosecond laser with spatial doughnut distribution," Chin. Opt. Lett. **18**, 013101 (2020).
10. T. Yang, H. Lin, and B. Jia, "Ultrafast direct laser writing of 2D materials for multifunctional photonics devices," Chin. Opt. Lett. **18**, 023601 (2020).
11. J. Bonse, S. Höhm, S. V. Kirner, A. Rosenfeld, and J. Krüger, "Laser-induced periodic surface structures—a scientific evergreen," IEEE J. Sel. Top. Quantum Electron. **23**, 9000615 (2016).
12. A. Y. Vorobyev and C. Guo, "Colorizing metals with femtosecond laser pulses," Appl. Phys. Lett. **92**, 041914 (2008).
13. B. Dusser, Z. Sagan, H. Soder, N. Faure, J.-P. Colombier, M. Jourlin, and E. Audouard, "Controlled nanostructrures formation by ultra fast laser pulses for color marking," Opt. Express **18**, 2913 (2010).
14. A.-M. Kietzig, M. Negar Mirvakili, S. Kamal, P. Englezos, and S. G. Hatzikiriakos, "Laser-patterned super-hydrophobic pure metallic substrates: Cassie to Wenzel wetting transitions," J. Adhesion Sci. Technol. **25**, 2789 (2011).
15. E. Rebollar, M. Castillejo, and T. A. Ezquerra, "Laser induced periodic surface structures on polymer films: from fundamentals to applications," Euro. Polym. J. **73**, 162 (2015).
16. A. Cunha, A.-M. Elie, L. Plawinski, A. P. Serro, A. M. B. do Rego, A. Almeida, M. C. Urdaci, M.-C. Durrieu, and R. Vilar, "Femtosecond laser surface texturing of titanium as a method to reduce the adhesion of *Staphylococcus aureus* and biofilm formation," Appl. Surf. Sci. **360**, 485 (2016).
17. J. Sipe, J. F. Young, J. Preston, and H. Van Driel, "Laser-induced periodic surface structure. I. Theory," Phys. Rev. B **27**, 1141 (1983).
18. J. Bonse, A. Rosenfeld, and J. Krüger, "On the role of surface plasmon polaritons in the formation of laser-induced periodic surface structures upon irradiation of silicon by femtosecond-laser pulses," J. Appl. Phys. **106**, 104910 (2009).
19. M. Huang, F. Zhao, Y. Cheng, N. Xu, and Z. Xu, "Origin of laser-induced near-subwavelength ripples: interference between surface plasmons and incident laser," ACS Nano **3**, 4062 (2009).
20. A. Borowiec and H. Haugen, "Subwavelength ripple formation on the surfaces of compound semiconductors irradiated with femtosecond laser pulses," Appl. Phys. Lett. **82**, 4462 (2003).
21. F. Costache, M. Henyk, and J. Reif, "Modification of dielectric surfaces with ultra-short laser pulses," Appl. Surf. Sci. **186**, 352 (2002).
22. Y. Dong and P. Molian, "Coulomb explosion-induced formation of highly oriented nanoparticles on thin films of 3C–SiC by the femtosecond pulsed laser," Appl. Phys. Lett. **84**, 10 (2004).
23. T. Crawford and H. Haugen, "Sub-wavelength surface structures on silicon irradiated by femtosecond laser pulses at 1300 and 2100 nm wavelengths," Appl. Surf. Sci. **253**, 4970 (2007).
24. G. Li, J. Li, Y. Hu, C. Zhang, X. Li, J. Chu, and W. Huang, "Femtosecond laser color marking stainless steel surface with different wavelengths," Appl. Phys. A **118**, 1189 (2015).
25. E. Hsu, T. Crawford, H. Tiedje, and H. Haugen, "Periodic surface structures on gallium phosphide after irradiation with 150 fs–7 ns laser pulses at 800 nm," Appl. Phys. Lett. **91**, 111102 (2007).
26. J. Bonse, S. Höhm, A. Rosenfeld, and J. Krüger, "Sub-100-nm laser-induced periodic surface structures upon irradiation of titanium by Ti:sapphire femtosecond laser pulses in air," Appl. Phys. A **110**, 547 (2013).
27. P. Gregorčič, M. Sedlaček, B. Podgornik, and J. Reif, "Formation of laser-induced periodic surface structures (LIPSS) on tool steel by multiple picosecond laser pulses of different polarizations," Appl. Surf. Sci. **387**, 698 (2016).
28. A. Vorobyev, V. Makin, and C. Guo, "Periodic ordering of random surface nanostructures induced by femtosecond laser pulses on metals," J. Appl. Phys. **101**, 034903 (2007).
29. S. Höhm, A. Rosenfeld, J. Krüger, and J. Bonse, "Laser-induced periodic surface structures on titanium upon single- and two-color femtosecond double-pulse irradiation," Opt. Express **23**, 25959 (2015).
30. M. Barberoglou, D. Gray, E. Magoulakis, C. Fotakis, P. Loukakos, and E. Stratakis, "Controlling ripples' periodicity using temporally delayed femtosecond laser double pulses," Opt. Express **21**, 18501 (2013).
31. A. Rosenfeld, M. Rohloff, S. Höhm, J. Krüger, and J. Bonse, "Formation of laser-induced periodic surface structures on fused silica upon multiple parallel polarized double-femtosecond-laser-pulse irradiation sequences," Appl. Surf. Sci. **258**, 9233 (2012).
32. W. Han, L. Jiang, X. Li, Q. Wang, H. Li, and Y. Lu, "Anisotropy modulations of femtosecond laser pulse induced periodic surface structures on silicon by adjusting double pulse delay," Opt. Express **22**, 15820 (2014).
33. J. Yao, C. Zhang, H. Liu, Q. Dai, L. Wu, S. Lan, A. V. Gopal, V. A. Trofimov, and T. M. Lysak, "Selective appearance of several laser-induced periodic surface structure patterns on a metal surface using structural colors produced by femtosecond laser pulses," Appl. Surf. Sci. **258**, 7625 (2012).
34. F. Fraggelakis, G. Mincuzzi, J. Lopez, I. Manek-Hönninger, and R. Kling, "Controlling 2D laser nano structuring over large area with double femtosecond pulses," Appl. Surf. Sci. **470**, 677 (2019).
35. F. Fraggelakis, G. Giannuzzi, C. Gaudiuso, I. Manek-Hönninger, G. Mincuzzi, A. Ancona, and R. Kling, "Double- and multi-femtosecond pulses produced by birefringent crystals for the generation of 2D laser-induced structures on a stainless steel surface," Materials **12**, 1257 (2019).
36. J. Liu, "Simple technique for measurements of pulsed Gaussian-beam spot sizes," Opt. Lett. **7**, 196 (1982).

37. D. W. Müller, T. Fox, P. G. Grützmacher, S. Suarez, and F. Mücklich, "Applying ultrashort pulsed direct laser interference patterning for functional surfaces," Sci. Rep. **10**, 3647 (2020).
38. V. Mitko, G. Römer, A. Huis, J. Skolski, J. Obona, V. Ocelík, and J. De Hosson, "Properties of high-frequency sub-wavelength ripples on stainless steel 304L under ultra short pulse laser irradiation," Phys. Procedia **12**, 99 (2011).
39. F. Fraggelakis, E. Stratakis, and P. Loukakos, "Control of periodic surface structures on silicon by combined temporal and polarization shaping of femtosecond laser pulses," Appl. Surf. Sci. **444**, 154 (2018).